3D Particle-In-Cell modeling of anomalous electron transport driven by the Electron Drift Instability in Hall thrusters

W Villafana, G Fubiani, L Garrigues, G Vigot, B Cuenot, O Vermorel

W Villafana, G Fubiani, L Garrigues, G Vigot, B Cuenot, et al.. 3D Particle-In-Cell modeling of anomalous electron transport driven by the Electron Drift Instability in Hall thrusters. 37th International Electric Propulsion Conference (IEPC-2022), Jun 2022, Boston, United States. hal-03855657

HAL Id: hal-03855657
https://hal.science/hal-03855657v1

3D Particle-In-Cell modeling of anomalous electron transport driven by the Electron Drift Instability in Hall thrusters

IEPC-2022-375

Presented at the 37th International Electric Propulsion Conference
Massachusetts Institute of Technology, Cambridge, MA, USA
June 19-23, 2022

W. Villafana [1] [2]
[1]*Centre Européen de Recherche et de Formation Avancée en Calcul Scientifique*
42 Av. Gaspard Coriolis, Toulouse, 31100, France
[2]*Princeton Plasma Physics Laboratory, Princeton, NJ, 08538 , USA*

G. Fubiani [3] and L. Garrigues [4]
Laboratoire Plasma et Conversion d'énergie, Université de Toulouse, Toulouse, 31077, France

G. Vigot [5]
Centre Européen de Recherche et de Formation Avancée en Calcul Scientifique
42 Av. Gaspard Coriolis, Toulouse, 31100, France
Centre National d'Etudes Spatiales, 18 avenue Edouard Belin, 31400 Toulouse, France
Safran Aircraft Engine, Campus de l'Espace, 1 avenue Hubert Curien,Vernon, 27207, France

B. Cuenot, [6] and O. Vermorel [7]
Centre Européen de Recherche et de Formation Avancée en Calcul Scientifique
42 Av. Gaspard Coriolis, Toulouse, 31100, France

Partially magnetized $\mathbf{E} \times \mathbf{B}$ discharges are highly coupled systems and subject to many plasma instabilities. In particular, the important electron drift velocity with respect to unmagnetized ions can lead to the growth and development of the Electron Drift Instability (EDI). The EDI has been the focus of extensive experimental, theoretical and numerical studies over the last two decades as it is suspected to play a role in the anomalous transport of electrons across the magnetic barrier. Despite significant progress, numerical investigations, mostly based on Particle-In-Cell modeling, have been mainly limited to 2D dimensional geometry due to the prohibitive computational cost of fully kinetic simulations. In this paper, we present the last developments of a 3D Particle-In-Cell study of a simplified Hall thruster allowing us to explore further the 3D structure of the EDI.

I. Introduction

In partially magnetized $\mathbf{E} \times \mathbf{B}$ plasmas, such as Hall thrusters (HT) [1, 2] or magnetrons [3, 4], it was observed that the electron transport across the magnetic barrier was surprisingly higher than expected [5]. Several physical mechanisms such as, for instance, plasma-wall interactions inducing secondary electron emission seem to contribute to this *anomalous transport* [6, 7]. However, coherent fluctuations of the electric field and plasma density in the $\mathbf{E} \times \mathbf{B}$ direction appear to be the main factor through particle-wave interactions [8].

---

[1] Former Postdoctoral researcher, Computational Fluid Dynamics Department
[2] Computational Research Associate, Plasma Science & Technology, wvillafa@pppl.gov
[3] CNRS researcher, GREPHE, gwenael.fubiani@cnrs.fr
[4] CNRS researcher, GREPHE, laurent.garrigues@laplace.univ-tlse.fr
[5] PhD. student, Computational Fluid Dynamics Department, vigot@cerfacs.fr
[6] Senior researcher, Computational Fluid Dynamics Department, cuenot@cerfacs.fr
[7] Senior researcher, Computational Fluid Dynamics Department, vermorel@cerfacs.fr

These fluctuations have been related to the Electron Drift Instability (EDI) and due to its kinetic nature, Particle-In-Cell simulations are well suited to describe them accurately. One-dimensional setups, in the $\mathbf{E} \times \mathbf{B}$ (azimuthal) direction [9, 10] could capture the EDI and provide first valuable insights about the anomalous transport. Unfortunately, 1D simulations cannot self-consistently compute the electric field in the axial direction, which needs to be imposed beforehand with a typical averaged value found in the system. A 2D axial-azimuthal PIC simulation does not suffer such a shortcoming and represents a significant improvement in a more accurate description of the EDI [11–15]. Nevertheless, recent work [16, 17] showed the presence of the walls in the radial direction could give rise to another kind of instability the Modified-Two-Stream-Instability (MTSI). A 2D radial-azimuthal PIC simulation showed that the MTSI could be coupled with the EDI, which might also affect the anomalous transport as a consequence. Unfortunately, like 1D setups, 2D radial-azimuthal configurations cannot self-consistently solve the axial electric field. Therefore a 3D study of the EDI seems to be necessary to obtain a more accurate description of the EDI.

Unfortunately, because of the computational cost, 3D PIC simulations remain rare with a few exceptions. Previous attempts either relaxed time and spatial constraints of the PIC method [18, 19], or considered miniaturized geometries [20, 21]. In the present work, we aim to keep realistic plasma parameters and length scales of a Hall thruster and to demonstrate the feasibility of 3D PIC simulations. To do so, two simulations of the same setup are considered. The first one is based on a structured grid using a state-of-the-art PIC code developed by LAPLACE laboratory. The second simulation is carried out with an unstructured framework using AVIP PIC, code that has been developed CERFACS laboratory. Traditionally, PIC studies rely on a regular mesh, as *self-forces* can lead to spurious results [22], including in a non-uniform grid. However, real configurations used in the industry might be unsuited for structured grids. They might even need further implementation efforts if the geometry is cylindrical or spherical. Thus, the present work will also attempt to assess the accuracy of results obtained with an unstructured grid using LAPLACE's results as a guide.

II. Numerical model and assumption

A. Computational domain

The computational domain consists of a slab representing a portion of the channel and a plume of a HT (no curvature is taken into account). As shown in Figure 1, the simulation domain presents a slight difference between CERFACS and LAPLACE. CERFACS takes advantage of its unstructured formulation with rounded edges at the channel exit with a local radius $L_R = 0.1\,\mathrm{cm}$ to avoid the unnecessary high electric field. In contrast, the Cartesian grid imposes to keep right-angled corners in LAPLACE's setup. The simulation is otherwise identical with axial and azimuthal lengths respectively given by $L_x = 2\,\mathrm{cm}$ and $L_y = 1.5\,\mathrm{cm}$. The radial gap is set to $L_z = 1.5\,\mathrm{cm}$.

Explicit PIC code must satisfy an important constraint on the space step Δx:

$$\Delta x \leq \lambda_D, \tag{1}$$

where λ_D is the Debye length:

$$\lambda_D = \sqrt{\varepsilon_0 k_B T_e n_e e^2} \tag{2}$$

with ε_0 the vacuum permittivity, k_B the Boltzmann constant, n_e the electron density and e the elementary charge. At steady state, we measure a Debye length $\lambda_D \approx 80\,\mu\mathrm{m}$ we the structured grid will use a uniform space step $\Delta x_{struct} = 78.125\,\mu\mathrm{m}$. For the unstructured mesh, the *Centaur* software [23] is used and the mesh is made of tetrahedral cells. The subsequent space step $\Delta x_{unstruct}$ is defined by

$$\Delta x_{unstruct} = V_c^{1/3}, \tag{3}$$

where V_c is the tetrahedral cell volume. In order to reduce mesh size, we set the averaged space step $\Delta x_{unstruct}$ to 70 µm in the channel region, i.e. the radial direction $z \in [1.25\,\mathrm{cm}; 2.75\,\mathrm{cm}]$ as shown on Figure 2 (a). In the plume region, for $z < 1.25\,\mathrm{cm}$ or $z > 2.75\,\mathrm{cm}$ (below and above the central region, we expect the Debye length to be greater as the density drops. Thus, we set $\Delta x_{unstruct} = 102\,\mu\mathrm{m}$.

B. Lagrangian kernel

The plasma is made of electrons and singly ionized ions $\mathrm{X_e}$ and is collisionless. The plasma is initialized with a standard Leap-Frog / Boris scheme for explicit PIC codes [24]. The number of macroparticles N_{ppc} is set to 40 in both simulations. For the unstructured grid, the statistical weight is automatically adjusted depending on the local cell

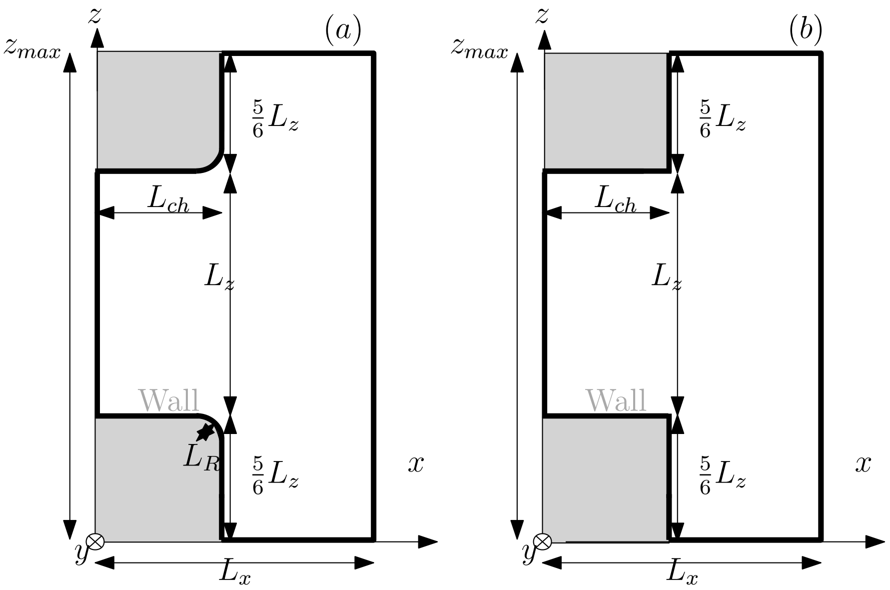

Figure 1 2D radial-axial $z-x$ view of the 3D setup of (a) the unstructured grid (for Cerfacs) and (b) the structured grid (for LAPLACE). The geometry is extruded over $1.5\,\mathrm{cm}$ in the azimuthal y direction.

volume. A statistical convergence study with $N_{ppc} = 100$ showed a difference of less than 10% on the final density, which was deemed for a preliminary study.The time step satisfies the stability condition [25] $\Delta t < 0.2\omega_{pe}$ and is set to $\Delta t = 1.25 \times 10^{-11}$ s.

In order to replace collision processes with neutrals, an imposed ionization source profile is used, similarly to what was done in previous 2D simulations [13, 14, 17]. The ionization profile unfiform in the azimuthal y direction and is given by:

$$\begin{cases} \text{if}(x,z) & \in [x_1,x_2]\times[z_1,z_2], \\ & S(x,z) = S_0\cos\left(\frac{x-x_m}{x_2-x_1}\right)\cos\left(\frac{z-z_m}{z_2-z_1}\right) \\ \text{else,} & S(x,z) = 0, \end{cases} \tag{4}$$

where S_0 is the strength of the source term. x_1, x_2 and z_1, z_2 are respectively the axial are radial limits of the ionization zone and are respectively set to $0.15, 0.75$cm and $1.25, 2.75$cm (the whole radial gap). The strength of the source term S_0 is implicitly computed at each time step by counting the total number of ions exiting the domain. For each ion leaving the domain, we inject a pair of ions/electrons according to the spatial profile given by Equation (4). At steady state $S_0 = 280\,\mathrm{A^2\,m^{-1}}$.

Particles leaving the domain are removed from the computation. At the anode (left side on Figure 2 (a)), the net electron current $\Gamma_e - \Gamma_i$ is calculated at each time step. This current is equal to electron flux injected at the cathode, located at $x = 1.9\,\mathrm{cm}$ inside the domain over a height $\Delta y = 8\,\mathrm{mm}$, similarly to the previous 2D PIC studies [13, 14]. The velocity of cathode electrons is sampled from a Maxwellian distribution with a preset temperature $T_{e,cathode} = 10\,\mathrm{eV}$.

C. Boundary conditions and field solver kernel

The boundary conditions are shown in Figure 2 (a). The anode is set to 300 V and the cathode (right side) is kept at 0 V. All other boundaries are modeled as dielectric following previous investigations [26]. For each node j at the dielectric boundary, the potential $\phi_{diel,j}$ is given by the net accumulated charge as follows:

$$\phi_{diel,j} = \frac{Q_{diel,j}}{C_{diel}}, \tag{5}$$

where $Q_{diel,j}$ is the total net charge updated at each time step for node j and $C_{diel} = 1 \times 10^{-6}\,\mathrm{F}$ is a numerical capacitance chosen beforehand for the whole simulation. The electric field is self-consistently computed by a home Poisson solver for the structured grid framework and by the external library Maphys [27] for AVIP PIC. Finally, the

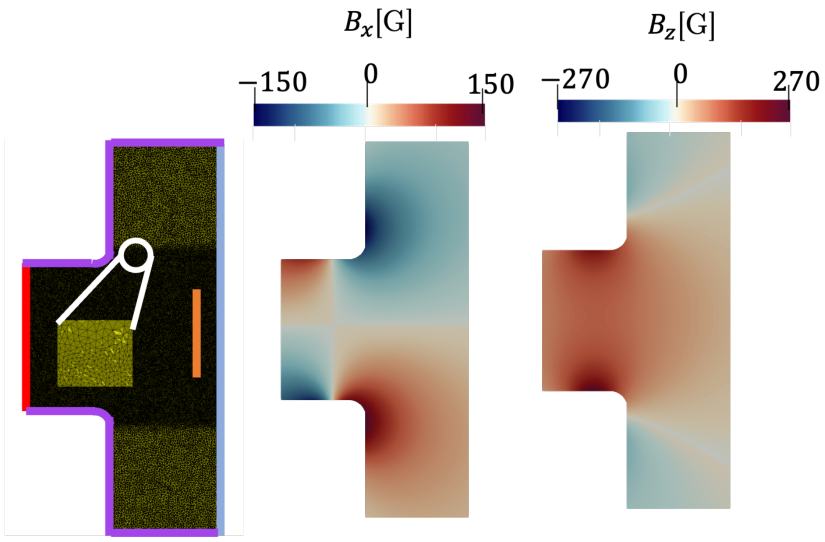

(a) (b) (c)

Figure 2 2D axial-radial view of boundary conditions and magnetic field. (a): Adaptive mesh used in AVIP PIC, with zoom inset. The left (red) boundary is the anode set at 300 V. Right (light blue) is the cathode set at 0 V. Electrons from the cathode are injected along the orange line. Other boundaries in purples are dielectric. (b): Axial B_x magnetic field topology. (c): Radial B_z magnetic field topology .

magnetic field is generated by two infinite wires in the azimuthal direction and located in the walls. The subsequent topology is 2D in the radial-axial plane and uniform in the azimuthal direction. It is maximum at the channel exit with 100 G.

III. Development and growth of the EDI

After a few microseconds of simulation, the plasma density in the ionization region rises. In the meantime, an initial wave leaves the channel and propagates toward the cathode, as seen in Figure 3 (first row). This feature was also observed in previous 2D simulations [14] and corresponds to the convection of ions that are accelerated under the potential drop between the two electrodes. In the channel the plasma density reaches levels above $2 \times 10^{18}\,\mathrm{m}^{-3}$, while in the plume, because of the plasma expansion in the radial direction, the density drops significantly near $2 \times 10^{17}\,\mathrm{m}^{-3}$. As early as 0.20 µs, azimuthal fluctuations appear in the channel region as show in Figure 3 (second row). Subtle at first, they are convected downstream into the plume. The measured wavelength is about 700 µm at 3.5 µs in the plume area.

Nonlinear effects strongly affect the dynamics of plasma instabilities but their study is also a formidable challenge [28]. A more practical approach consists in focusing on the early growth of the instability. The observed azimuthal fluctuations seem to be related to the EDI. To investigate this assumption, we can rely on the corresponding 3D dispersion relation, derived by Ducrocq *et al.* [29] as shown in Equation (6).

$$\begin{aligned} 1k^2\lambda_D^2\, \mathrm{g}\left(\frac{\omega - k_y V_d}{\Omega_{ce}}, \left(k_x^2\; k_y^2\right) r_L^2, k_z^2\rho^2\right) \\ - \frac{k^2\lambda_D^2\omega_{pi}^2}{\left(\omega - k_x v_p\right)^2} = 0, \end{aligned} \tag{6}$$

where λ_D is the Debye length, $\omega_p i$ the ion plasma frequency, Ω_{ce} the cyclotron frequency, $V_d = E_x B_y$ the electron drift velocity, r_L the Larmor radius of electrons, v_p the velocity of the ion beam and k_x, k_y and k_z the axial, azimuthal and

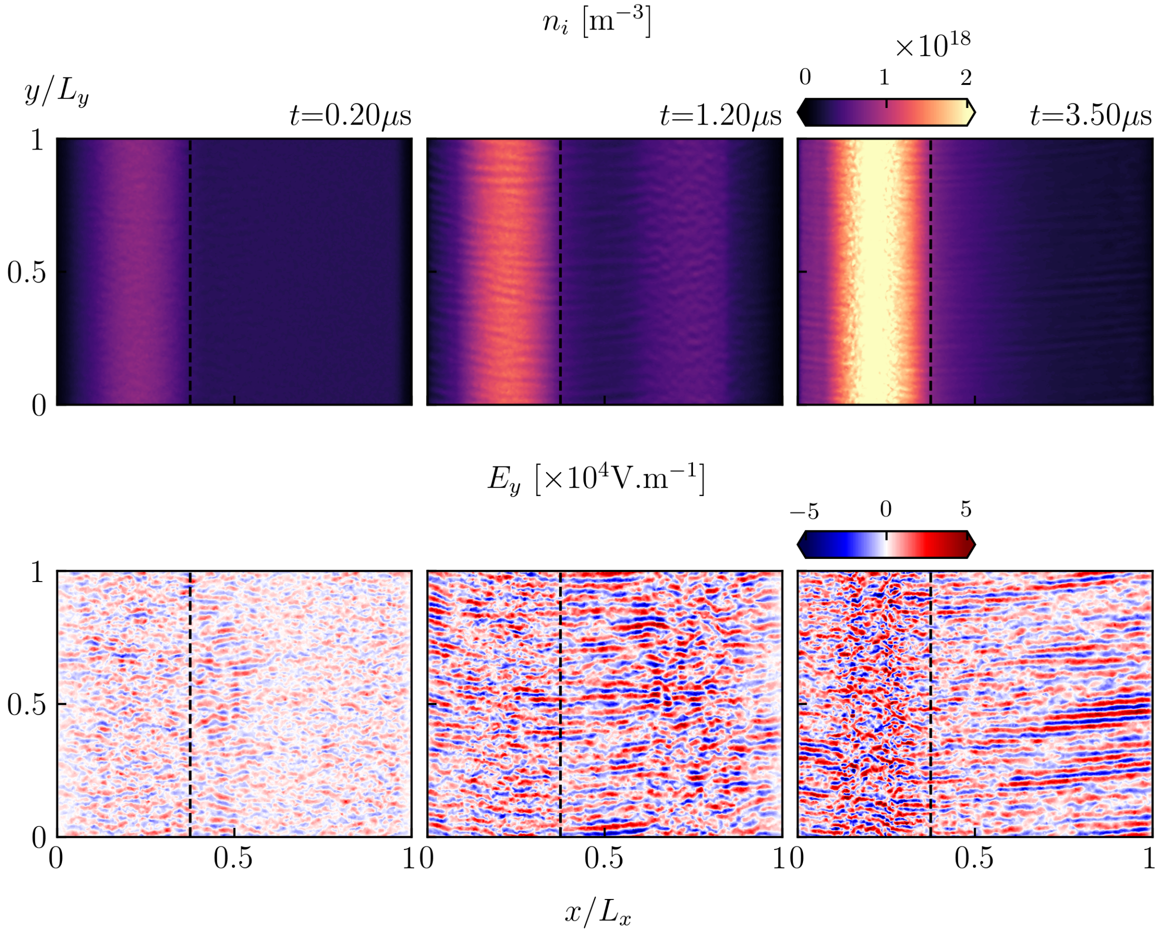

Figure 3 Timeline of variables of interest in the centered axial-azimuthal $x-y$ **plane at** $z = z_{max}2 = 2\,\mathrm{cm}$**. Top row: ion density** n_i**; bottom row: azimuthal electric field** E_y**. Each column corresponds to a specific time:** $t = 0.20, 1.20$ **and** $3.50\,\mu\mathrm{s}$**. The dashed black line represents the channel exit at** $x = 0.375L_x = 0.75\,\mathrm{cm}$**. The proportions between the** x **and** y **directions are conserved.**

radial components of the wavenumber $\mathbf{k}$. The Gordeev function $g\Omega, X, Y$ [30] can be expressed in two ways:

$$\begin{aligned} g\Omega, X, Y &= i\Omega_0^\infty e^{-X1-\cos(\varphi)-\frac{1}{2}Y\varphi^2 i\Omega\varphi}\mathrm{d}\varphi, \\ &= \frac{\Omega}{\sqrt{2Y}}\mathrm{e}^{-X}{}_{m=-\infty}^{\infty} \mathrm{Z}\left(\frac{\Omega-m}{\sqrt{2Y}}\right)\mathrm{I}_m X, \end{aligned} \tag{7}$$

where I_m is the modified Bessel function of the first kind and Z is the plasma dispersion function. Equation (6) can be solved with an iterative scheme proposed by Cavalier *et al.* [31] using the plasma dispersion function from Python `Plasmpy` package [32]. To calculate the complex frequency $\omega\mathbf{k}$, Equation (6) takes the wave number $\mathbf{k}$ and local plasma conditions such as the ion density n_i, axial electric field E_x, radial magnetic field B_y and electron temperature T_e an ion velocity $v_{i,x}$, as inputs. For the present case, local plasma conditions are measured, before the development of azimuthal fluctuations, at $t = 50\,\mathrm{ns}$ in the axial-azimuthal plane located at $z = 2\,\mathrm{cm}$ at the axial position $x = 0.16L_x = 0.32\,\mathrm{cm}$. It is assumed the fluctuations do not propagate in the axial direction so $k_x = 0$. The radial wavenumber k_z is set to $2\pi L_z$, which corresponds to the geometric constraint in the channel region. The resulting growth rate γ, given by the imaginary part of $\omega\mathbf{k}$ is presented in Figure 4 (a). On Figure 4 (a), the numerical growth rate γ_{num} obtained in AVIP PIC is also reported. To compute the latter, the fastest growing mode was first identified in the 1D FFT performed in the azimuthal direction at the same axial position $x = 0.32\,\mathrm{cm}$. Then, the linear phase growth of the instability was determined in Figure 4 (b); and finally a least square interpolation provided the slope, which is equal to $2\gamma_{num}$. Overall, the numerical growth rate γ_{num} fairly agrees with the theory, which suggests the present instability is the EDI. A similar dimensionless wavenumber $k_y\lambda_D$ is obtained in both cases but the growth rate is over-predicted in the theory by a factor of three. The apparent discrepancy might be explained by the fact that the present simulation does not have the same initial assumptions made in Ducrocq *et al.*'s work. For instance, the magnetic field is assumed purely radial in Ducrocq *et al.*, whereas it also has an axial component B_x in the PIC simulation. Although $B_x = 0$ in the considered axial-azimuthal plane, it reaches a comparable magnitude of B_z when approaching the walls. We also recall that in previous 2D [16, 17] simulations, the magnetic field was purely radial which probably helped to get a better agreement with Ducrocq *et al.*'s model.Thus, at this point of our investigations, it is believed that the presence of a 2D magnetic field topology is responsible for the observed discrepancy, and further investigations would be required to assess that assumption. However, given the relatively fair agreement between the numerical and theoretical growth rate, we are also confident the present instability is probably the EDI.

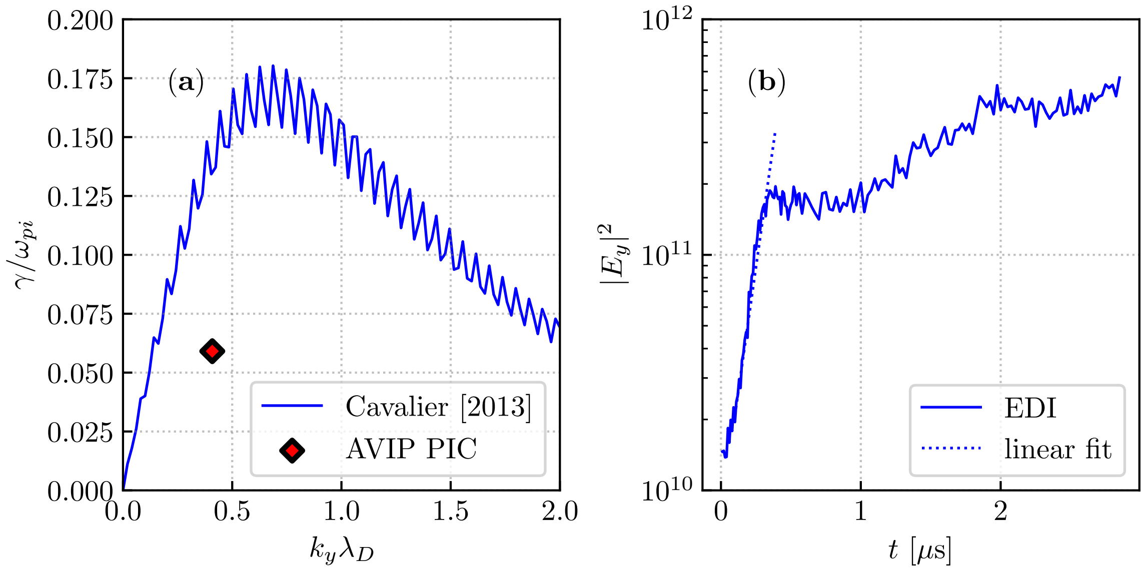

Figure 4 Growth and temporal evolution of the EDI-ion acoustic instability. (a): comparison of the dimensionless growth rate $\gamma\omega_{pi}$ (labeled as "AVIP PIC") measured in the $x = 0.16L_x$ plane with linear theory (blue from Cavalier *et al.* [31]). The theoretical growth rate is obtained using $T_e = 13.8\,\mathrm{eV}$, $E_x = 10\,\mathrm{kV\,m^{-1}}$, $B_z = 95\,\mathrm{G}$ and $n_i = 5\times10^{17}\,\mathrm{m^{-3}}$. (b): temporal evolution of the dominant azimuthal wavenumber $k_y = 10\,021\,\mathrm{rad\,m^{-1}}$ at the axial location $x = 0.16L_x = 0.32\,\mathrm{cm}$. The dotted lines indicate the linear regression obtained with a least square method during the exponential growth of the instability

IV. Steady state

The steady-state is reached in approximately 20 µs when electron and ion fluxes become equal at the dielectric boundary. The final injection current in the ionization zone then stabilizes at $280\,\mathrm{A^2\,m^{-1}}$. In the channel, Figure 5 (a) shows the density is the highest in the ionization region with n_i $4\times10^{17}\,\mathrm{m^{-3}}$ before expanding into the plume. Interesting filaments are visible in both the channel and in the plume. They seem related to the azimuthal fluctuations discussed in Section III as we shall see in Figure 6. The electron temperature T_e is maximum at the channel exit with T_e 70 eV (see Figure 5 (b). The hottest area has an arc shape, ~40 mm wide in the axial direction at the centerline and approximately twice shorter near the walls, probably due to losses at the dielectric layer. Figure 5 (c) indicates that ions are accelerated at the channel exit, which is also responsible for the rise in temperature. The maximum electric field at the channel exit is around $50\,\mathrm{kV\,m^{-1}}$. In the channel region, the short wavelengths from Section III are still propagating in the azimuthal direction. Overall, the normal working point of a Hall thruster is retrieved.

It is easier to study the previously discussed azimuthal fluctuations by analyzing the azimuthal electric field in 3D in Figure 6. As illustrated in Figure 6 (a) and (b)), clear short wavelengths of approximately $\lambda_w \approx 650 - 700\,\mu\mathrm{m}$ are visible. In earlier studies [8], it was proposed that the EDI transitions to an ion acoustic wave. In such a case,

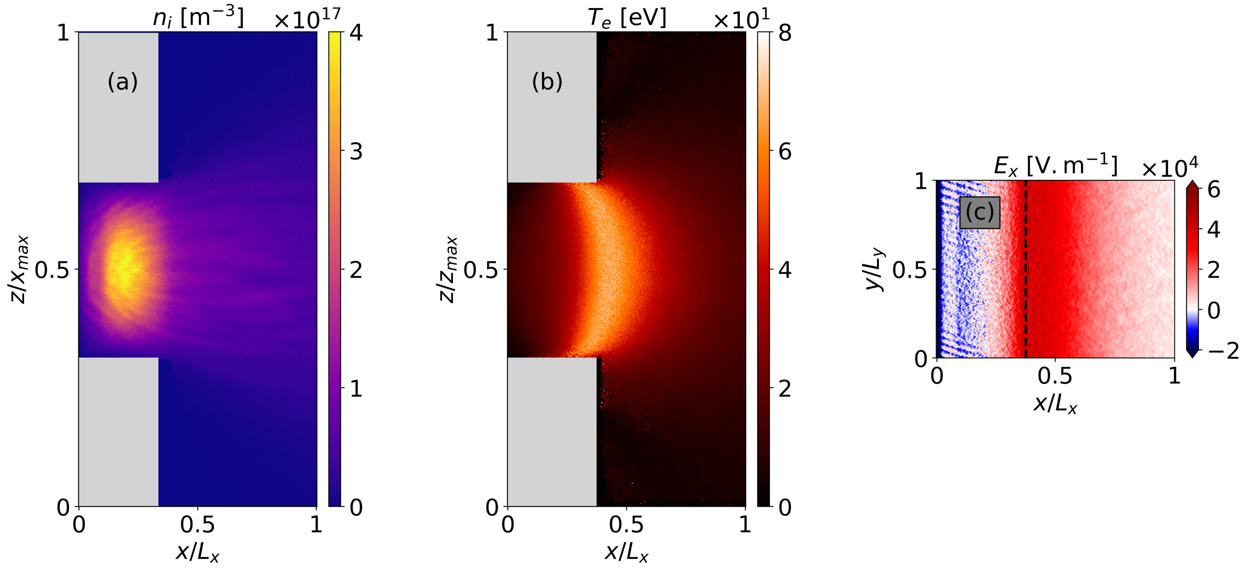

Figure 5 2D maps at $t = 20\mu s$ with a structured grid. (a): axial-radial cross section view of ion density n_i at the centered plane $y = L_y/2 = 0.75\,\mathrm{cm}$. (b): axial-radial cross section view of electron temperature T_e at the centered plane $y = L_y/2 = 0.75\,\mathrm{cm}$. (c): axial-azimuthal cross section view of axial electric field E_x at $z = z_{max}/2 = 2\,\mathrm{cm}$. The dashed line corresponds to the channel's exit. Aspect ratio has been respected for each 2D map.

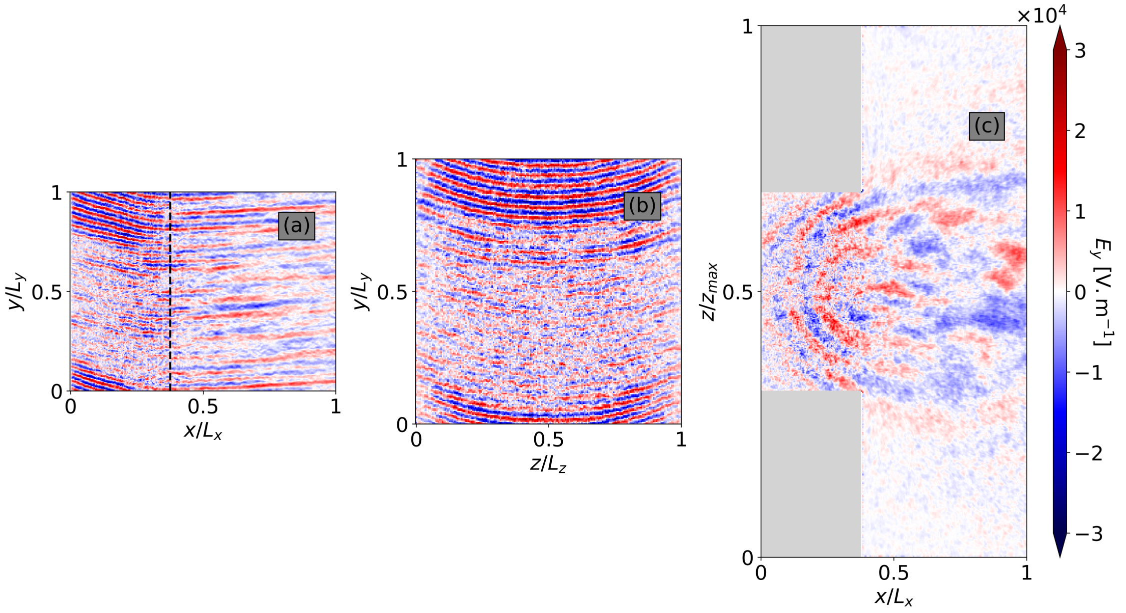

Figure 6 Azimuthal Electric field with a structured grid at $t = 20\mu s$. (a): axial-azimuthal cross section view at $z = z_{max}/2 = 2\,\mathrm{cm}$, the dashed black line corresponds to the channel's exit. (b): axial-radial cross section view at channel exit, i.e. $x = 0.375L_x = 0.75\,\mathrm{cm}$. (c): axial-radial cross section view at the centered plane $y = L_y/2 = 0.75\,\mathrm{cm}$. Aspect ratio has been respected for each 2D map.

the resulting ion-acoustic wave roughly scales with $2\pi\sqrt{2}\lambda_D \approx 9\lambda_D$. Given that $\lambda_D \approx 80\,\mu\mathrm{m}$ in the channel, it seems that as in 2D—[13, 14], the EDI has transitioned to an ion acoustic wave. We also note that a larger azimuthal fluctuation in Figure 6 (a-b), enveloping the ion-acoustic wave seems to be present. The corresponding wavelength is around $\lambda_{w,large} = L_y \sim 190\Lambda_D$. Over $0.25L_y$, the ion acoustic wave is clearly defined with an amplitude of $\sim 30\,\mathrm{kV\,m^{-1}}$.

Over the remaining part of the azimuthal direction, the ion-acoustic wave seems much weaker and shows less spatial coherence.

The instability also displays an interesting structure in the axial-radial plane as shown in Figure 6 (c)). In the channel, the wave presents a non-negligible axial wavenumber k_x with a corresponding wavelength of $\sim 2.5\,\mathrm{mm}$. The axial-azimuthal view in Figure 6 (a) and Figure 5 (c) also showed such an axial component but this feature has not been extensively studied in the literature. Downstream the channel exit, the wave loses its axial structure but seems to expand in the radial direction. It is suspected to be responsible for the filaments observed in Figure 5 (a). However, because the density drops significantly, no clear patterns can be sustained far away from the central region.

V. Conclusion and future work

In this paper, we presented the latest progress regarding a fully 3D PIC study of a portion of a Hall thruster including dielectric walls and a typial 2D magnetic field topology. In particular, we focused our attention on the growth and development of the EDI, an important parameter driving the anomalous electron transport across the magnetic barrier. Preliminary results showed that both a structured and unstructured framework could this instability. Its growth can be approximated by linear theory and the EDI transitions to an ion acoustic wave at steady state, similarly to what was observed in previous 2D numerical studies. Besides, the normal working point of a Hall thruster was retrieved.

Among future work, it is planned to perform a more detailed quantitative comparison between using a structured and unstructured grid. Such a work will be achieved by defining identical postprocessing and post-processing procedures, which should also lay out new guidelines for the community. In particular, the effects of using a coarsening grid in AVIP PIC will be assessed.

Acknowledgments

W. Villafana acknowledges financial support from a Safran Aircraft Engines doctoral research award as well as from the Association Nationale de la Recherche et de la Technologie (ANRT) as part of a CIFRE convention. From his side, G. Vigot acknowledges the support from the French Space Agency: CNES (Centre National d'Études Spatiales) and Safran Aircraft Engine as financial contributors in accordance with the EPIC convention. This work has been partially funded by ANR (n° ANR-16-CHIN-003- 01) and Safran Aircraft Engines within the project POSEIDON. This work used the HPC resources of IDRIS/TGCC/CINES under the allocation A0102A06074 made by GENCI.

References

[1] Boniface, C., Garrigues, L., Hagelaar, G. J. M., Boeuf, J. P., Gawron, D., and Mazouffre, S., "Anomalous cross field electron transport in a Hall effect thruster," *Applied Physics Letters*, Vol. 89, No. 16, 2006, p. 161503. https://doi.org/10.1063/1.2360182, URL https://doi.org/10.1063/1.2360182.

[2] Smirnov, A. N., Raitses, Y., and Fisch, N. J., "Electron cross-field transport in a miniaturized cylindrical Hall thruster," *IEEE Transactions on Plasma Science*, Vol. 34, No. 2, 2006, pp. 132–141. https://doi.org/10.1109/TPS.2006.872185.

[3] Tsikata, S., and Minea, T., "Modulated Electron Cyclotron Drift Instability in a High-Power Pulsed Magnetron Discharge," *Phys. Rev. Lett.*, Vol. 114, 2015, p. 185001. https://doi.org/10.1103/PhysRevLett.114.185001, URL https://link.aps.org/doi/10.1103/PhysRevLett.114.185001.

[4] Boeuf, J.-P., and Chaudhury, B., "Rotating Instability in Low-Temperature Magnetized Plasmas," *Phys. Rev. Lett.*, Vol. 111, 2013, p. 155005. https://doi.org/10.1103/PhysRevLett.111.155005, URL https://link.aps.org/doi/10.1103/PhysRevLett.111.155005.

[5] Meezan, N., Hargus, W., and Cappelli, M., "Anomalous electron mobility in a coaxial Hall discharge plasma," *Physical review. E, Statistical, nonlinear, and soft matter physics*, Vol. 63, 2001, p. 026410. https://doi.org/10.1103/PhysRevE.63.026410.

[6] Garrigues, L., Hagelaar, G. J. M., Boniface, C., and Boeuf, J. P., "Anomalous conductivity and secondary electron emission in Hall effect thrusters," *Journal of Applied Physics*, Vol. 100, No. 12, 2006, p. 123301. https://doi.org/10.1063/1.2401773, URL https://doi.org/10.1063/1.2401773.

[7] Sydorenko, D., Smolyakov, A., Kaganovich, I., and Raitses, Y., "Kinetic simulation of secondary electron emission effects in Hall thrusters," *Physics of Plasmas*, Vol. 13, No. 1, 2006, p. 014501.

[8] Lafleur, T., Baalrud, S. D., and Chabert, P., "Theory for the anomalous electron transport in Hall effect thrusters. II. Kinetic model," *Physics of Plasmas*, Vol. 23, No. 5, 2016, p. 053503. https://doi.org/10.1063/1.4948496, URL https://doi.org/10.1063/1.4948496.

[9] Lafleur, T., Baalrud, S. D., and Chabert, P., “Theory for the anomalous electron transport in Hall effect thrusters. I. Insights from particle-in-cell simulations,” *Physics of Plasmas*, Vol. 23, No. 5, 2016, p. 053502. https://doi.org/10.1063/1.4948495, URL https://doi.org/10.1063/1.4948495.

[10] Janhunen, S., Smolyakov, A., Chapurin, O., Sydorenko, D., Kaganovich, I., and Raitses, Y., “Nonlinear structures and anomalous transport in partially magnetized ExB plasmas,” *Physics of Plasmas*, Vol. 25, No. 1, 2018, p. 011608. https://doi.org/10.1063/1.5001206, URL https://doi.org/10.1063/1.5001206.

[11] Adam, J., Héron, A., and Laval, G., “Study of stationary plasma thrusters using two-dimensional fully kinetic simulations,” *Physics of Plasmas*, Vol. 11, No. 1, 2004, pp. 295–305.

[12] Lafleur, T., and Chabert, P., “The role of instability-enhanced friction on ‘anomalous’ electron and ion transport in Hall-effect thrusters,” *Plasma Sources Science and Technology*, Vol. 27, No. 1, 2017, p. 015003.

[13] Boeuf, J. P., and Garrigues, L., “ExB electron drift instability in Hall thrusters: Particle-in-cell simulations vs. theory,” *Physics of Plasmas*, Vol. 25, No. 6, 2018, p. 061204. https://doi.org/10.1063/1.5017033, URL https://doi.org/10.1063/1.5017033.

[14] Charoy, T., Boeuf, J. P., Bourdon, A., Carlsson, J. A., Chabert, P., Cuenot, B., Eremin, D., Garrigues, L., Hara, K., Kaganovich, I. D., Powis, A. T., Smolyakov, A., Sydorenko, D., Tavant, A., Vermorel, O., and Villafana, W., “2D axial-azimuthal particle-in-cell benchmark for low-temperature partially magnetized plasmas,” *Plasma Sources Science and Technology*, Vol. 28, No. 10, 2019, p. 105010. https://doi.org/10.1088/1361-6595/ab46c5, URL https://doi.org/10.1088%2F1361-6595%2Fab46c5.

[15] Coche, P., and Garrigues, L., “A two-dimensional (azimuthal-axial) particle-in-cell model of a Hall thruster,” *Physics of Plasmas*, Vol. 21, No. 2, 2014, p. 023503.

[16] Janhunen, S., Smolyakov, A., Sydorenko, D., Jimenez, M., Kaganovich, I., and Raitses, Y., “Evolution of the electron cyclotron drift instability in two-dimensions,” *Physics of Plasmas*, Vol. 25, No. 8, 2018, p. 082308. https://doi.org/10.1063/1.5033896, URL https://doi.org/10.1063/1.5033896.

[17] Villafana, W., Petronio, F., Denig, A. C., Jimenez, M. J., Eremin, D., Garrigues, L., Taccogna, F., Alvarez-Laguna, A., Boeuf, J.-P., Bourdon, A., Chabert, P., Charoy, T., Cuenot, B., Hara, K., Péchereau, F., Smolyakov, A. I., Sydorenko, D., Tavant, A., and Vermorel, O., “2D radial-azimuthal particle-in-cell benchmark for E x B discharges,” *Plasma Sources Science and Technology*, 2021. https://doi.org/10.1088/1361-6595/ac0a4a, URL https://doi.org/10.1088/1361-6595/ac0a4a.

[18] Hirakawa, M., and Arakawa, Y., “Particle simulation of plasma phenomena in Hall thrusters,” *Proceedings of the 24th International Electric Propulsion Conference*, 1995, pp. 95–164.

[19] Hirakawa, M., and Arakawa, Y., “Numerical simulation of plasma particle behavior in a Hall thruster,” *32nd Joint Propulsion Conference and Exhibit*, 1996, p. 3195.

[20] Taccogna, F., and Minelli, P., “Three-dimensional particle-in-cell model of Hall thruster: The discharge channel,” *Physics of Plasmas*, Vol. 25, No. 6, 2018, p. 061208. https://doi.org/10.1063/1.5023482, URL https://doi.org/10.1063/1.5023482.

[21] Minelli, P., and Taccogna, F., “How to build PIC-MCC models for Hall microthrusters,” *IEEE Transactions on plasma science*, Vol. 46, No. 2, 2017, pp. 219–224.

[22] Colella, P., and Norgaard, P. C., “Controlling self-force errors at refinement boundaries for AMR-PIC,” *Journal of Computational Physics*, Vol. 229, No. 4, 2010, pp. 947–957.

[23] Borras, P., Clement, D., Despeyroux, T., Incerpi, J., Kahn, G., Lang, B., and Pascual, V., “Centaur: The System,” *SIGSOFT Softw. Eng. Notes*, Vol. 13, No. 5, 1988, p. 14–24. https://doi.org/10.1145/64137.65005, URL https://doi.org/10.1145/64137.65005.

[24] Boris, J. P., “Relativistic plasma simulation-optimization of a hybrid code,” *Proc. Fourth Conf. Num. Sim. Plasmas*, 1970, pp. 3–67.

[25] Birdsall, C. K., “Particle-in-cell charged-particle simulations, plus Monte Carlo collisions with neutral atoms, PIC-MCC,” *IEEE Transactions on Plasma Science*, Vol. 19, No. 2, 1991, pp. 65–85. https://doi.org/10.1109/27.106800.

[26] Fubiani, G., Agnello, R., Furno, I., Garrigues, L., Guittienne, P., Hagelaar, G., Howling, A., Jacquier, R., Reman, B., Simonin, A., and Taccogna, F., “Negative hydrogen ion dynamics inside the plasma volume of a linear device: Estimates from particle-in-cell calculations,” *Physics of Plasmas*, Vol. 28, No. 6, 2021, p. 063503. https://doi.org/10.1063/5.0044358, URL https://aip.scitation.org/doi/10.1063/5.0044358.

[27] Agullo, E., Giraud, L., and Poirel, L., "Robust Preconditioners via Generalized Eigenproblems for Hybrid Sparse Linear Solvers," *SIAM Journal on Matrix Analysis and Applications*, Vol. 40, No. 2, 2019, pp. 417–439. https://doi.org/10.1137/17M1153765, URL https://doi.org/10.1137/17M1153765.

[28] Lampe, M., Manheimer, W. M., McBride, J. B., Orens, J. H., Shanny, R., and Sudan, R., "Nonlinear development of the beam-cyclotron instability," *Physical Review Letters*, Vol. 26, No. 20, 1971, p. 1221.

[29] Ducrocq, A., Adam, J., Héron, A., and Laval, G., "High-frequency electron drift instability in the cross-field configuration of Hall thrusters," *Physics of Plasmas*, Vol. 13, No. 10, 2006, p. 102111.

[30] Gordeev G. V., *KETP*, 1952, p. 660.

[31] Cavalier, J., Lemoine, N., Bonhomme, G., Tsikata, S., Honoré, C., and Grésillon, D., "Hall thruster plasma fluctuations identified as the ExB electron drift instability: Modeling and fitting on experimental data," *Physics of Plasmas*, Vol. 20, No. 8, 2013, p. 082107. https://doi.org/10.1063/1.4817743, URL https://doi.org/10.1063/1.4817743.

[32] Community, P., Everson, E., Stańczak, D., Murphy, N. A., Kozlowski, P. M., Malhotra, R., Langendorf, S. J., Leonard, A. J., Stansby, D., Haggerty, C. C., Mumford, S. J., Beckers, J. P., Bedmutha, M. S., Bergeron, J., Bessi, L., Bryant, K., Carroll, S., Chambers, S., Chattopadhyay, A., Choubey, A., Deal, J., Diaz, D., Díaz Pérez, R., Einhorn, L., Fan, T., Farid, S. I., Goudeau, G., Guidoni, S., Hansen, R. S., Heuer, P., Hillairet, J., How, P. Z., Huang, Y.-M., Humphrey, N., Isupova, M., Kent, J., Kulshrestha, S., Kuszaj, P., Lim, P. L., Magarde, A., Martinelli, J. V., Munn, J., Parashar, T., Patel, N., Polak, J., Rao, A., Raj, R., Rajashekar, V., Savcheva, A., Shen, C., Sherpa, D. N., Silva, F., Singh, A., Singh, A., Sipőcz, B., Tavant, A., Varnish, T., Vo, A., Xu, S., Zhang, C., Du, T., Qudsi, R., Richardson, S., Skinner, C., Modi, D., Drozdov, D., and Montes, K., "PlasmaPy," , Mar. 2021. https://doi.org/10.5281/zenodo.4602818, URL https://doi.org/10.5281/zenodo.4602818, The development of PlasmaPy has been partially supported by the U.S. National Science Foundation, the U.S. Department of Energy, NASA, and the Smithsonian Institution.